Analysis of flow field design on vanadium redox flow battery performance: development of 3D computational fluid dynamic model and experimental validation

M. Messaggi, M. Zago*, P. Canzi, R. Mereu, A. Baricci, F. Inzoli, A. Casalegno

Politecnico di Milano, Department of Energy, Via Lambruschini 4, 20156 Milano, Italy

* corresponding author: matteo.zago@polimi.it

Abstract

Homogeneous distribution of the electrolyte over the porous electrode is a critical issue hindering the commercialization of vanadium redox flow batteries, owing to increased overpotential at high current and limited power density of the system. Therefore, an understanding of the physical phenomena regulating mass transport of the electrolyte is crucial to improving system performance. The present work describes the development and experimental validation of a 3D computational fluid dynamic model of a vanadium redox flow battery in a half-cell configuration with an active area of 25 cm^2. The model simulates the influence of a single serpentine and an interdigitated flow field. The adoption of the half-cell configuration allows the negative electrode to be considered as a pseudo-reference electrode with zero potential loss, leading to a reduction in computation time and the number of fitting parameters, which can be determined with reduced uncertainty. The developed model includes a traditional fluid dynamic analysis of the electrolyte in the flow field and in the porous electrode, coupled with the electrochemistry of the reactions involved. In both the experiments and the simulations, the single serpentine distributor exhibits better performance and higher pressure drops compared to those of the interdigitated geometry under all the investigated operating conditions. In the analysis of the local reaction rate, both distributors experienced increased reaction rates under the rib, induced by a by-pass flow between adjacent channels.

The reaction rate shows a highly heterogeneous distribution in the serpentine geometry, while it is more uniform in the interdigitated configuration.

Keywords: CFD, interdigitated, model, serpentine, VRFB.

Nomenclature

List of symbols

a	Active area [m^{-1}]
k_0	Reaction rate constant [m s^{-1}]
D	Diffusivity of vanadium ions [m^2 s^{-1}]
R_d	HSO_4^- Dissociation rate [mol m^{-3}]
$\boldsymbol{u}$	Velocity vector [m s^{-1}]
$\boldsymbol{f}$	Volume force vector [N m^{-3}]
N	Species molar flux [mol m^{-2} s^{-1}]
F	Faraday constant [A s mol^{-1}]
u_i	Species mobility [mol s kg^{-1}]
R	Universal gas constant [J mol^{-1} K^{-1}]
T	Temperature [K]
z	Charge number [-]
c	Molar concentration [mol m^{-3}]
i	Current density [A m^{-2}]
i_R	Reaction rate [A m^{-3}]
E	Equilibrium potential [V]
V	Voltage [V]
h_m	Mass transport coefficient [m s^{-1}]
x	Mass fraction [-]
MM	Molar mass [kg $kmol^{-1}$]
M	Molarity [mol l^{-1}]
P	Power [W]
Q	Flow rate [m^3 s^{-1}]
p	Pressure [Pa]
A_{cell}	Electrode area [cm^2]

Greek symbols

α	Charge transfer coefficient [-]
ε	Porosity of compressed electrode [-]
κ	Permeability [m^2]
ρ	Density [kg m^{-3}]
μ	Viscosity [Pa s]
β_F	Forchheimer drag coefficient [m^{-1}]
ϕ	Potential [V]
η^*	Overpotential [V]
η	Efficiency [-]

Superscripts

eff	Effective properties
0	Standard conditions
b	Relative to bulk
s	Relative to surface
T	Transposed
C	Relative to cathode

Subscripts

H^+	Relative to protons
SO_4^{2-}	Relative to sulphate ions

HSO_4^-	Relative to hydrogen sulphate ions
V^{4+}	Relative to VO^{2+} ion (Vanadium IV)
V^{5+}	Relative to VO_2^+ ion (Vanadium IV)
i	Relative to i-th chemical species
m	Relative to mass
R	Relative to electrochemical reactions
s	Relative to solid phase
l	Relative to electrolyte
C	Relative to cathode

Glossary

CFD	Computational fluid dynamics
EIS	Electrochemical impedance spectroscopy
OCV	Open circuit voltage
PRESTO!	Pressure staggering options
SIMPLE	Semi implicit method for pressure linked equations
SoC	State of charge
VRFB	Vanadium redox flow battery

1. Introduction

The vanadium redox flow battery (VRFB) is a promising technology for energy storage due to its unique separation of power and energy, its high efficiency, and its extremely long charge/discharge cycle life [1–4]. The VRFB employs the same element at different oxidation states in both electrodes, thus avoiding the issue of permanent contamination between the two half-cell electrolytes [5]. However, the commercialization of VRFBs continues to be hindered by technological issues, among which the mass transport of the electrolyte over the porous electrode is one of the most important [4,6], as it leads to increased overpotential at high current and limits the power density of the system [7,8]. Therefore, understanding the main physical phenomena regulating VRFB operation and quantifying the corresponding performance losses are crucial to achieving market competitiveness. Moreover, the interplay between fluid dynamics in the distribution channels and the morphology of the porous electrode is not well understood at the local level throughout the active area of the cell, where local reactant starvation may occur, and further limit the system performance and lifetime.

One powerful tool to achieve a more solid understanding of the mass transport phenomena is computational fluid dynamics (CFD) code [9], which allows flexible simulations of system operation with different flow rates, state of charge (SoC), material properties, and distributor channels. These simulations can determine the impact of these parameters on the distribution of physical quantities, such as potentials, pressure drops, local velocities, and concentrations. This versatile tool, when properly coupled with a rigorous experimental validation of the results over a wide range of operating conditions and flow field geometries, can provide insight into the mass transport issues in VRFBs and help to design innovative flow fields in order to mitigate mass transport losses.

Various modelling analyses of VRFBs with the aid of CFD can be found in the literature, but most of these consider a very simple straight geometry, in some cases without channels, which is quite different from the actual flow field configuration adopted in real applications. In most cases, this configuration leads to a uniform distribution of the variables in one direction, reducing the 3D model to a 2D model. This allows an understanding of the electrochemical and transport phenomena that characterise the operation of the flow battery, but fails to provide insight into the complex fluid dynamics and mass transport phenomena that occur in channels and porous media, such as the under-the-rib fluxes or realistic pressure drop estimations of a distributor configuration.

Oh et al. [10] developed a 3D non-isothermal and transient model of an all-vanadium flow battery in order to reproduce the charge and discharge curves of the battery and the local potential profiles through the electrode. The model considers a simple straight geometry composed only of a current collector and a porous electrode, without any channels and with a reduced active area of 4 cm^2. Migration, vanadium crossover, and side reactions are neglected, and the dilute-solution approximation is used to describe species transport.

Ma et al. [11] presented a 3D stationary isothermal model of a V(II,III) half-cell flow battery validated against simulation data taken from the literature. They analysed the distribution of velocity, overpotential, vanadium concentration, and current density on different planes of a 13.8 cm^2 porous electrode without a flow field, neglecting the migration effect and describing species transport with a dilute-solution approximation.

Wang and Cho [12] coupled a 3D dynamic non-isothermal model of an all-vanadium flow battery with electrolyte tanks in order to simulate charge and discharge curves, and validated it against experimental data from the literature. The evolution of the temperature, concentration, and current density distributions over time, along with the corresponding characteristic times, were analysed. The domain was composed of only current collectors, electrodes (100 cm^2), and a membrane, with no channels, and with a direct inlet/outlet of vanadium in the electrode side boundaries. The dilute-solution approximation was made, side reactions were ignored, and the mass transport resistance in pores of the electrode was neglected. Moreover, the conditions appeared to be uniform along one direction of the domain, effectively reducing the 3D model to a 2D model.

Chen et al. [13] built a 3D transient model of a flow field with a parallel configuration to investigate only the fluid dynamics of the flow, and compared the model with experimental data acquired by optical investigation of the flow field during operation. An experimental evaluation of the performance was carried out, without comparison to any modelling activity.

Ozgoli et al. [14] developed 2D and 3D models to analyse hydrodynamic and electrochemical phenomena. The 2D model was used to evaluate the distribution of vanadium in the electrodes and the potential profiles through the electrodes and the membrane. A sensitivity analysis was also performed with respect to the physical properties of the electrodes and membrane. In the 3D model, the study was focused on the evaluation of the fluid dynamic behaviour inside porous

electrodes with different inlet/outlet configurations in order to determine the best configuration in terms of performance and pressure drop.

The state of art for the CFD modelling of VRFBs is represented by [15,16], which describe the development of a model for an all-vanadium flow battery that analysed the effect of the flow field pattern on the performance and local distribution of the main physical quantities. In [15] the authors simulated a reduced geometry for both the positive and negative electrodes with an interdigitated flow field configuration, explored different inlet/outlet layouts, and evaluated their effects on performance and on the distribution of the potentials, current density, and pressure, and their homogeneity. A sensitivity analysis was also performed on the geometrical dimensions of the channels and flow rate, and the results were validated experimentally. In [16], Xu et al. considered different distributor in a complete 3D model. Batteries without a flow field and with serpentine and parallel patterns were analysed in terms of their performance, overpotentials, pressure drops, and the uniformity of the physical quantities along the distributor, and a sensitivity analysis was performed on the flow rate. The authors also defined a global efficiency for each geometry, and determined that the serpentine flow field was the best of the three simulated fields in terms of heterogeneity and global efficiency.

To the authors' knowledge, solid and extensive experimental validations of such models are scarce, but such evaluations are fundamental to ensure the reliability of the modelled results in quantifying local physical phenomena and in performing sensitivity analyses. In this work, the investigation is focused on a CFD simulation of the positive electrode of a vanadium flow battery in the half cell configuration (VO_2^+/VO^{2+}-H_2) with two realistic flow field designs: a serpentine and an interdigitated geometry. The model simulations are extensively and rigorously validated with the corresponding experimental data under different operating conditions. The number of fitting parameters is limited in order to increase the reliability of the estimation of physical quantities and the comparison between the adopted flow field geometries.

The work is organised as follows: the experimental setup and the experimental tests are described in Section 2, and then, in Section 3 model development is presented in Section 3. Section 4 first reports the experimental data. Subsequently, after a detailed description of the approach used for model validation, the main modelling results are presented, highlighting local heterogeneities during operation. Finally, some conclusions are given in Section 5.

2. Experimental

2.1 Experimental setup

The experimental tests were performed using a modified cell architecture [17], in which the negative electrode was fed with hydrogen for use as the counter and reference electrode, and the positive electrode was fed with a liquid electrolyte consisting of water, sulfuric acid (i.e., H^+, HSO_4^- and SO_4^{2-}), and the charged vanadium ions VO^{2+} and VO_2^+. The reactions occurring in discharge mode at the negative and positive electrode were, respectively:

$$\frac{1}{2}H_2 \longrightarrow H^+ + e^- \quad \text{(I)}$$

$$VO_2^+ + 2H^+ + e^- \longrightarrow VO^{2+} + H_2O \quad \text{(II)}$$

During the charging cycle, these reactions were reversed. In this cell architecture, the negative electrode acts as a pseudo-reference electrode; thus, the measured voltage difference is mainly related to the positive electrode overpotential and ohmic loss, leading to a reduction in the number of fitting parameters necessary for model validation.

The active area of the cell was 25±0.5 cm^2. A single serpentine graphite distributor was used at the negative electrode, while the positive electrode was fed with a single serpentine or an interdigitated flow field.

The membrane was Nafion® 115, the positive electrode was SGL 39 AA carbon paper (nominal thickness of ~290 μm, compressed to 230 μm), and the negative electrode was commercial

Pt/C (Pt loading 0.6 mg cm^{-2}) coated on a diffusion layer. The cell temperature was maintained at an ambient temperature of 23 ± 2 °C.

A pulse dampener [18,19] was used in the hydraulic circuit of the positive electrolyte to eliminate flow rate fluctuations induced by the peristaltic pump (Watson-Marlow 323Du with a 4 roller head pump), and a pressure transducer (Druck PMP1400, accuracy ±0.15% of pressure) was utilised to measure the pressure loss between the cell inlet and outlet. The positive electrolyte solution was prepared by mixing 69.75 g of vanadium IV sulphate oxide hydrate (Alfa Aesar) with 300 ml of 5 M sulfuric acid[1] (Fischer Chemicals), in order to obtain a 1 M solution of vanadium ions. This electrolyte was chosen to provide a sufficient quantity of the solution to perform tests, assuming a constant SoC during the whole test. Additionally, the bottle containing the electrolyte was pressurised with N_2 in order to avoid air infiltration. The flow rate of the fully humidified hydrogen was controlled and measured using a calibrated flow controller (Brooks Instrument, uncertainty: 0.7% of rate + 0.001 nl min^{-1}).

A potentiostat (Material Mates 540-R, current range 10A to -30A, voltage range -12V to +12V, accuracy 0.1% + 0.2% f.s.) was used to measure the polarization curves and high frequency resistance of the electrochemical impedance spectra in the frequency range of 30 kHz to 1 kHz.

2.2 Experimental tests

The single electrode performance was evaluated using polarization curves at different electrolyte flow rates and vanadium SoC in order to highlight the effect of the mass transport phenomena on the performance of the VRFB positive electrode fed with either the single serpentine or interdigitated flow field.

[1] The molarity of sulfuric acid was chosen based on the solubility study reported in [33], in which 5 M sulphuric acid was found to be a suitable concentration for 1 M vanadyl sulphate at 20 °C.

The adopted cell architecture eliminated the cross-contamination effects induced by the mixing of the positive and negative electrolytes that usually occurs in vanadium flow batteries [17]. However, vanadium permeation through the membrane, which could lead to a mixed-potential at the negative electrode [20] and alter the hydrogen equilibrium potential, still occurred. In order to limit this effect, the polarization curves were measured only in discharge mode, in which vanadium flux though the membrane was hindered by the liquid phase potential gradients, which suppress the transport of VO^{2+} and VO_2^+ from the positive to the negative electrode [21].

In order to obtain reliable and repeatable polarization curves, the following experimental procedure was adopted. Before each polarization, the vanadium circuit pump was stopped for 5 min. During this time the hydrogen flow rate was set to 90 ml min^{-1}, corresponding to a current of 12.9 A, which guaranteed a great excess of the reactants. Subsequently, the pump was switched on and the OCV was measured for 45 s to verify and monitor the initial SoC. The polarization curve was then acquired as a one-way curve with increasing current. The current density was increased in steps of 0.05 A cm^{-2}, with each step being held for 45 s, and a cell voltage limit of 0.7 V. During the processing of the raw experimental data, the initial transient voltage response of each step was excluded from the analysis, and the average value of the remaining voltage data was considered.

The polarization curves reported in this work were measured at 3 different electrolyte flow rates (10, 20 and 60 ml min^{-1}) and two different SoC (0.9 and 0.6). Each polarization was performed at least twice to verify the repeatability of the measurement.

3. Model

3.1 Model development and assumptions

A custom model of a VRFB, coupling fluid dynamics and electrochemistry, was developed with the aid of a commercial fluid dynamics code.

The model domain, depicted in Fig. 1, represents the positive electrode of the VRFB and was composed of a distributor channel, which feeds the reactants to a porous carbon electrode where electrochemical reactions occur. A polymer membrane then allows the transport of protons from the positive electrode to the negative side of the battery; the latter was not modelled in the present work.

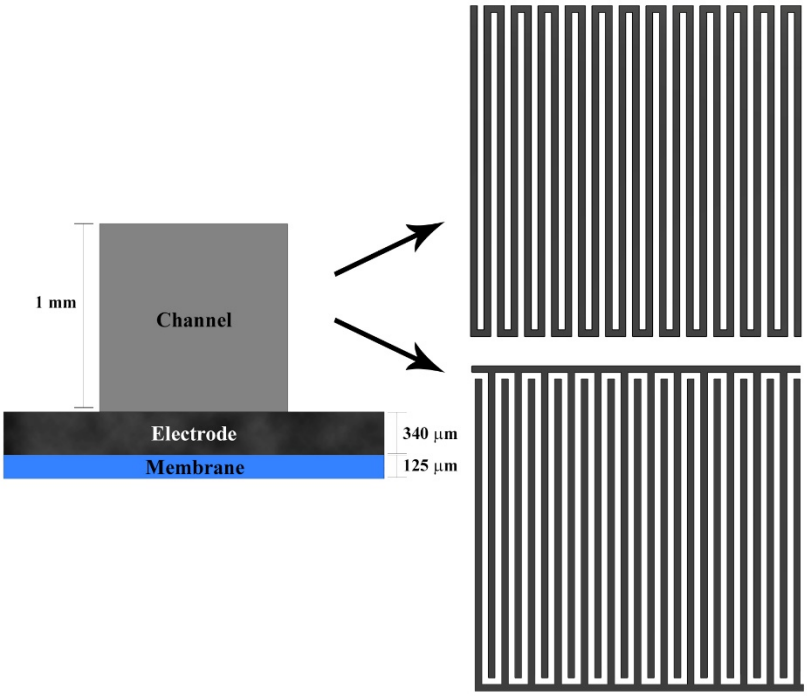

Fig. 1 – Model domain and simulated flow fields.

The main electrochemical reaction occurring at the positive electrode is the electrochemical reduction (discharge mode) or oxidation (charge mode) of VO_2^+ (Eq. II), but the two-step dissociation of sulphuric acid also takes place:

$$H_2SO_4 \leftrightarrow HSO_4^- + H^+ \quad \text{(III)}$$

$$HSO_4^- \leftrightarrow SO_4^{2-} + H^+ \quad \text{(IV)}$$

As described in [22], the first step (Eq. III) was neglected in this work because the products are favoured, while the second step (Eq. IV) was modelled as an additional source of H^+, given by:

$$\mathrm{R_d} = k_d \left(\frac{c_{H^+} - c_{SO_4^-}}{c_{H^+} + c_{SO_4^-}} - \beta \right) \quad (1)$$

where k_d and β are constants taken from [22] and the corresponding values are reported in Table 2.

The main assumptions of the model are listed below:

- Stationary model.
- Isothermal model.
- Parasitic reactions, such as hydrogen and oxygen evolution, are neglected.
- Incompressible fluid.
- Isotropic properties for the electrode and membrane.
- Electrolyte physical properties not dependent on the state of charge.
- Membrane is only permeable to protons.
- Complete wettability of the membrane.
- Electroneutrality of the membrane and solutions.

3.2 Mass balance

The conservation of mass was computed in the channel and the porous electrode:

$$\rho \nabla \cdot \boldsymbol{u} = \mathrm{S_m} \quad (2)$$

where ρ is the density of the electrolyte (constant), $\boldsymbol{u}$ the velocity, and S_m the source term that takes into account the electrochemical reactions, occurring only inside the porous electrode.

3.3 Momentum balance

The conservation of momentum was computed according to the Navier-Stokes equation (Eq. 3), in the channel, and the Brinkmann equation (Eq. 4), in porous media, in order to achieve a smooth transition of the velocity profile between these two domains:

$$\nabla \cdot (\rho \boldsymbol{u}\boldsymbol{u}) = -\nabla p + \nabla \cdot \left[\mu\left(\nabla \boldsymbol{u} + (\nabla \boldsymbol{u})^T\right)\right] + \boldsymbol{f} \tag{3}$$

$$\frac{1}{\varepsilon^2}\nabla \cdot (\rho \boldsymbol{u}\boldsymbol{u}) = -\nabla p + \nabla \cdot \left[\frac{\mu}{\varepsilon}\left(\nabla \boldsymbol{u} + (\nabla \boldsymbol{u})^T\right)\right] - \frac{2\mu}{3\varepsilon}\nabla(\nabla \cdot \boldsymbol{u}) - \left(\frac{\mu}{\kappa} + \beta_F|\boldsymbol{u}| + S_m\right)\boldsymbol{u} + \boldsymbol{f} \tag{4}$$

where ε is the porosity of the porous medium, p is the pressure, μ the dynamic viscosity of the fluid, κ the permeability of the porous medium. β_F is the Forchheimer drag coefficient, which was neglected in the present work, and $\boldsymbol{f}$ is the volume force vector, which is zero as gravity is not taken into account.

3.4 Species balance

The conservation of each species was solved in all fluid domains according to (Eq. 5):

$$\nabla \cdot \boldsymbol{N}_i = S_i \tag{5}$$

where S_i is the species molar source (Eq. 6-8), depending on the reaction rate of the electrochemical reactions i_R, which is discussed in Section 3.5, and on the dissociation rate, which was neglected in the present work.

$$S_{V^{4+}} = -\frac{i_R}{F} \tag{6}$$

$$S_{V^{5+}} = \frac{i_R}{F} \tag{7}$$

$$S_{H^+} = \frac{2i_R}{F} \tag{8}$$

The molar flux $\boldsymbol{N}_i$ was computed according to the Nernst-Planck equation, which describes the molar flux of each species as a combination of diffusive, migrative, and convective contributions.

$$\boldsymbol{N}_i = -D_i^{eff}\nabla c_i - z_i u_i c_i F\nabla\phi_l + \boldsymbol{u}c_i \tag{9}$$

where the index *i* indicates the species, D_i^{eff} is the effective diffusivity, c_i is the molar concentration, z_i is the charge number, u_i is the mobility calculated according to the Nernst-Einstein equation (Eq. 12), F is the Faraday constant, and ϕ_l is the potential of the liquid phase. The Nernst-Plank equation does not have to be solved for one of the species as a result of the electroneutrality principle:

$$\sum_i z_i c_i = 0 \tag{10}$$

The effective diffusivity was obtained by correcting the species diffusivity with the effect of the porosity, according to the Bruggeman correction:

$$D_i^{eff} = \varepsilon^{3/2} D_i \tag{11}$$

The equation used to obtain the value of mobility was [23]:

$$u_i = \frac{D_i^{eff}}{RT} \tag{12}$$

Proton flux through the membrane was not modelled, while the electrolytic potential was solved as discussed in Section 3.5.

3.5 Charge balance

Charge conservation (Eq. 13-14) was solved in all the domains, using a non-zero source term only in the porous electrode where electrochemical reactions occur.

$$\nabla\cdot i_l = S_R \tag{13}$$

$$\nabla\cdot i_s = -S_R \tag{14}$$

where i_s is the current density in the solid phase and i_l is the current density inside the liquid electrolyte phase.

$$i_s = -\sigma_s^{eff} \nabla \phi_s \tag{15}$$

$$i_l = F \sum_i z_i \boldsymbol{N}_i = F \sum_i z_i \left(- D_i^{eff} \nabla c_i - z_i u_i c_i F \nabla \phi_l + \boldsymbol{u} c_i \right) \quad \text{(in electrolyte)} \tag{16}$$

$$i_l = -\sigma_l \nabla \phi_l \quad \text{(in membrane)} \tag{17}$$

where $\sigma_s^{eff} = (1-\varepsilon)^{3/2} \sigma_s$ is the effective electric conductivity of the solid phase and σ_l is the protonic conductivity of the membrane.

The source term in the porous electrode is the reaction rate obtained according to the Butler-Volmer kinetic model:

$$S_R = i_R \tag{18}$$

$$i_R = k_0 a F \left(c^s_{V^{4+}} \cdot e^{\frac{\alpha F \eta^*}{RT}} - c^s_{V^{5+}} \cdot e^{\frac{\alpha F \eta^*}{RT}} \right) \tag{19}$$

where k_0 is the reaction rate constant, a is the specific surface area, α is the charge transfer coefficient, T is the temperature, the c_i^s terms are the concentrations of vanadium IV and V on the surface of the electrode, and $\eta^* = \phi_s - \phi_l - E_{eq}$ is the overpotential, where $E_{eq} = E_C^{0'} + \frac{RT}{F} \ln\left(c_{H^+}^{C\ 2} \right)$ is the equilibrium potential of the reaction between vanadium and hydrogen.

The concentration of vanadium on the surface of the electrode can be determined from the bulk concentration using a convective mass transport model (Eq. 20) with a mass transport coefficient h_m obtained according to [24](Eq. 21).

$$-h_m \left(c^s_{V4+} - c^b_{V4+} \right) = \frac{i_R}{aF} \quad , \quad h_m \left(c^s_{V5+} - c^b_{V5+} \right) = \frac{i_R}{aF} \tag{20}$$

$$h_m = 1.6 \cdot 10^{-4} \boldsymbol{u}^{0.4} \tag{21}$$

Including Eq. 19, it is possible to rearrange Eq. 18 as follows:

$$i_R = \frac{k_0 aF}{1+\frac{k_0}{h_m}\cdot\left(e^{\frac{\alpha F\eta^*}{RT}}+e^{-\frac{(1-\alpha)F\eta^*}{RT}}\right)}\left(c^b_{V^{4+}}\cdot e^{\frac{\alpha F\eta^*}{RT}}-c^b_{V^{5+}}\cdot e^{-\frac{(1-\alpha)F\eta^*}{RT}}\right) \tag{22}$$

3.6 Boundary conditions

At the inlet of the distributor channel, the mass fraction of each species (Eq. 23) was set along with a uniform flow velocity value depending on the chosen volumetric flow rate.

The mass fraction values depend on the SoC of the electrolyte; that is, the concentration of the vanadium (IV,V) species, and the molarity of the solutions, according to Eqs. 24-27:

$$x_i = \frac{c_i \cdot MM_i}{\rho} \tag{23}$$

$$c_{V^{4+}} = (1-SoC)\cdot M_V \tag{24}$$

$$c_{V^{5+}} = SoC\cdot M_V \tag{25}$$

$$c_{H^+} = M_{acid} - (1-SoC)\cdot M_V \tag{26}$$

$$c_{HSO_4^-} = M_{acid} + M_V \tag{27}$$

At the outlet of the channel, the pressure gauge value is set to zero as a reference.

The electric potential on the contact areas between the electrode and the current collector (not present in the computational domain) was set according to the working point selected for the simulation. An electrolytic potential of zero was set at the anodic boundary of the membrane in order to simulate the presence of the hydrogen side of the half-cell configuration. The interface between the membrane and the porous electrode was impermeable to all species and to electrons, while the continuity of the electrolytic potential and flux was ensured between these adjacent regions. All the remaining boundaries were treated as walls impermeable to all physical quantities.

3.7 Software setup

The model was developed in ANSYS® Fluent 17 using several custom user defined functions (UDFs) for the implementation of the electrochemistry, along with the standard fluid dynamics module. The solver setup used was a SIMPLE algorithm for velocity-pressure coupling, with a second order upwind scheme for the spatial discretisation of equations, except for the resolution of the pressure, which used a PRESTO! scheme.

3.8 Analysis of the mesh

For all the investigated configurations of the distributor channel, a hexahedral structured mesh was used, with 457900 elements for the serpentine and 538200 cells for the interdigitated geometry. The mesh was refined in the porous layer, where higher gradients develop, and in the zones of the flow field, where high velocity gradients are expected, in order to obtain better accuracy.

An analysis of meshes with different grades of refinement, i.e. a coarser and a finer grid, was also carried out through the calculation of the *Grid Convergence Index* (GCI) for different quantities to ensure the independence of the solution from the spatial discretization used. The result of this analysis showed that for the mesh used in the present work, the error band was lower than 1% with respect to the asymptotic solution for all the investigated physical quantities. Further refinement of the mesh could lead to lower error bands, but would increase the computational time of the simulations.

4. Results and discussion

4.1 Experimental results

Figure 2a illustrates the measured polarization curves at SoC 0.6 for a single serpentine and an interdigitated flow field. When the flow rate was fixed, the single serpentine configuration

clearly exhibited higher performance at all the investigated operating conditions. The measurement reproducibility is reported in Appendix A; the data at SoC 0.9 are not reported for the sake of brevity, since the performance behaviour was the same. However, as shown in Fig. 2b, the single serpentine geometry resulted in greater pressure drops than those of the interdigitated one, especially at 60 ml min^{-1}.

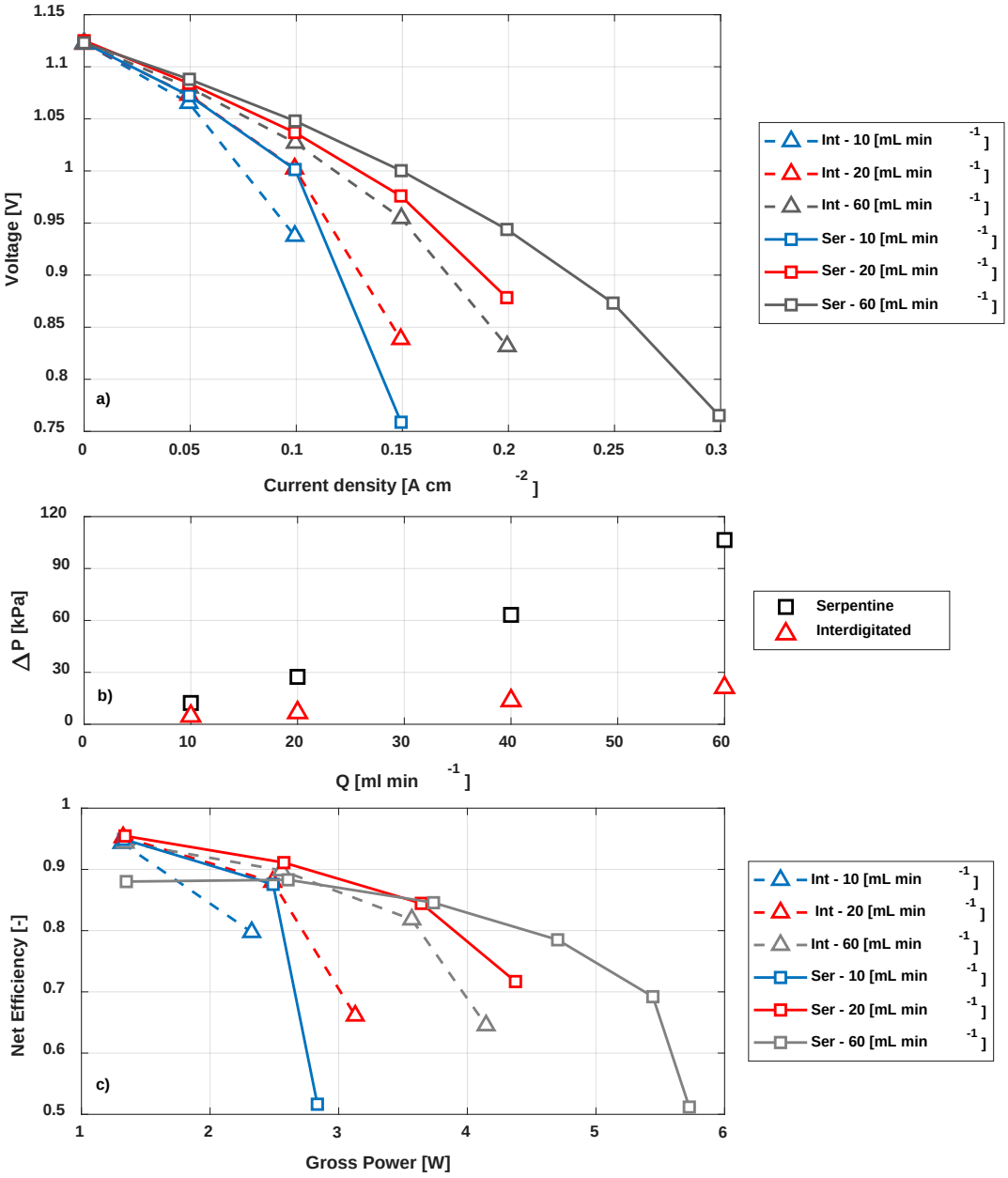

Fig. 2 – a) Experimental polarization curves at SoC 0.6; b) measured pressure drops; c) net efficiency.

The pressure drops directly affect the auxiliary energy consumption. As reported in [25], the pumping power can be calculated as:

$$P_{pump} = \frac{Q \cdot \Delta p}{\eta_{pump}} \tag{27}$$

Assuming a pump efficiency (η_{pump}) of 0.9, the corresponding power consumption values for a single serpentine and interdigitated flow field are reported in Table 1.

Table 1 – Auxiliary power consumption in mW for a 25 cm² electrode.

Flow rate [ml min^{-1}]	**Single serpentine [mW]**	**Interdigitated [mW]**
10	2.30	0.88
20	10.4	2.53
40	47.2	10.15
60	118.3	23.56

At a high flow rate, the pumping power associated with the single serpentine configuration is considerably higher than that of the interdigitated one. Therefore, it is more effective to compare the performance of different distributors considering their different pressure drops (i.e. auxiliary consumption), rather than at the same flow rate. By calculating the gross power produced by the cell and the power consumption of the pumping system, the net efficiency of the system can be defined as:

$$\eta_{net} = \frac{V_{cell} i_{cell} A_{cell} - P_{pump}}{V_{cell} i_{cell} A_{cell}} \tag{28}$$

As shown in Fig. 2c, under the investigated operating conditions, the single serpentine configuration outperformed the interdigitated system at high gross power, in terms of net efficiency, while at low gross power values, the interdigitated configuration exhibited a slightly better performance.

The optimal flow field has not been conclusively established in the literature [18,25], as benchmark parameters and operating conditions to allow consistent comparisons among different works have not been established. In [26], the interdigitated configuration outperformed the single serpentine configuration, while in [27] the single serpentine configuration exhibited the best performance. The influence of the flow field is affected by various physical parameters, such as the active area of the cell, the electrode porosity and permeability, and the stoichiometry of the reactants. Moreover, there is a strong interplay among these physical quantities. The main aim of the present modelling analysis is to validate the developed model for different flow field configurations under a wide range of operating conditions, while limiting the number of fitting parameters. This should increase the reliability of the results and provide insight into the most relevant physical phenomena governing the operation of the system, and should also permit the elucidation of the interplay between the fluid dynamics in the distribution channels and the electrode morphology at the local level.

4.2 Model results

4.2.1 Model validation

Adoption of the half-cell configuration allowed the number of fitting parameters to be reduced. Since the negative electrode was modelled as a pseudo-reference electrode, the corresponding potential loss can be considered to be zero. The model was calibrated with respect to the polarization curves performed at 20 ml min^{-1} and SoC 0.6. As depicted in Fig. 3, acceptable agreement between the simulations and the experiments was observed. The assumed and fitted model parameters are reported in Table 2. Most of the parameters have been taken from the literature. Only the membrane conductivity σ, specific area a, and reaction rate constant k_0 were fitted, and the resulting values were consistent with those reported in the literature [16]. Since the computational time of each operating point is high (nearly 1 h), a limited number of fitting

parameters were chosen. Only those which were found to have the greatest influence on the polarization curves based on sensitivity analysis were considered. Better agreement between the model and the experiment could be obtained by adjusting other parameters, such as the diffusivities and the transfer coefficient slightly, but this is out of the scope of this work.

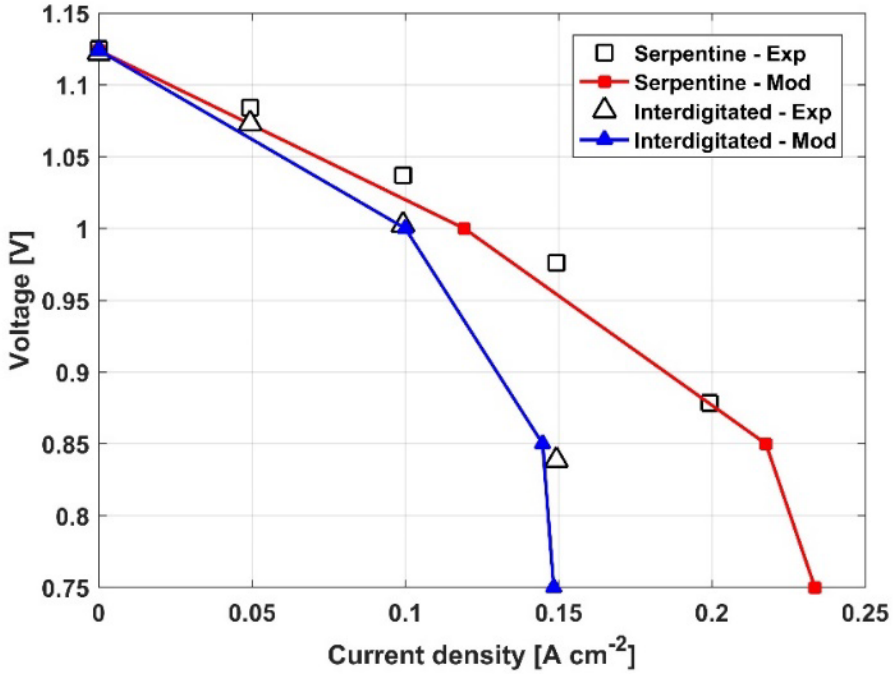

Fig. 3 – Comparison of the simulated and measured polarization curves at 20 ml min^{-1} and SoC 0.6.

Subsequently, model simulations were performed using the model parameters in Table 2 and flow rates of 10 ml min^{-1} (Fig. 4a) and 60 ml min^{-1} (Fig. 4b). The model was able to reproduce the experimental data qualitatively and quantitatively for both flow rates, indicating that the main physical phenomena were correctly described. Only at 60 ml min^{-1} and high current densities did the discrepancy between the model and the experiments become more evident. This was probably due to the difference between the simulated and the experimental pressure drops or an overestimation of the local convective mass transport coefficient in the pores of the electrodes, which could be remedied by improving the correlation reported in [24] and adopted in this work by further analytical work. Moreover, the model was also able to reproduce the

measured pressure losses (Fig. 4c). A similar relationship between the modelling and experimental results was previously reported in [26], in which the model simulations underestimated the experimental results for the interdigitated geometry, while the opposite occurred for the single serpentine geometry.

Table 2 – Parameters used in the model.

Parameter	**Value**	**Reference**
Active area a [m^{-1}]	17000	fitted
Reaction rate constant k_0 [m s^{-1}]	7e-6	fitted
Charge transfer coefficient α [-]	0.5	[28]
Porosity [-]	0.88	manufacturer
Porosity of compressed electrode ε [-]	0.859	
Permeability κ [m^2]	1.75e-11	[22]
Density ρ [kg m^{-3}]	1350	[22]
Viscosity μ [Pa s]	0.005	[22]
Diffusivity of vanadium ions D_{V+} [m^2 s^{-1}]	3.9e-10	[22]
Diffusivity of protons D_{H+} [m^2 s^{-1}]	9.312e-9	[22]
Diffusivity of hydrogen sulphate ions D_{HSO4-} [m^2 s^{-1}]	1.33e-9	[22]
Diffusivity of sulphate ions D_{SO4^2-} [m^2 s^{-1}]	1.065e-9	[22]
HSO_4^- Dissociation rate constant k_d [s^{-1}]	1e-4	[22]
HSO_4^- Degree of dissociation β [-]	0.25	[22]
Membrane conductivity σ_m [S m^{-1}]	2	exp. fitted

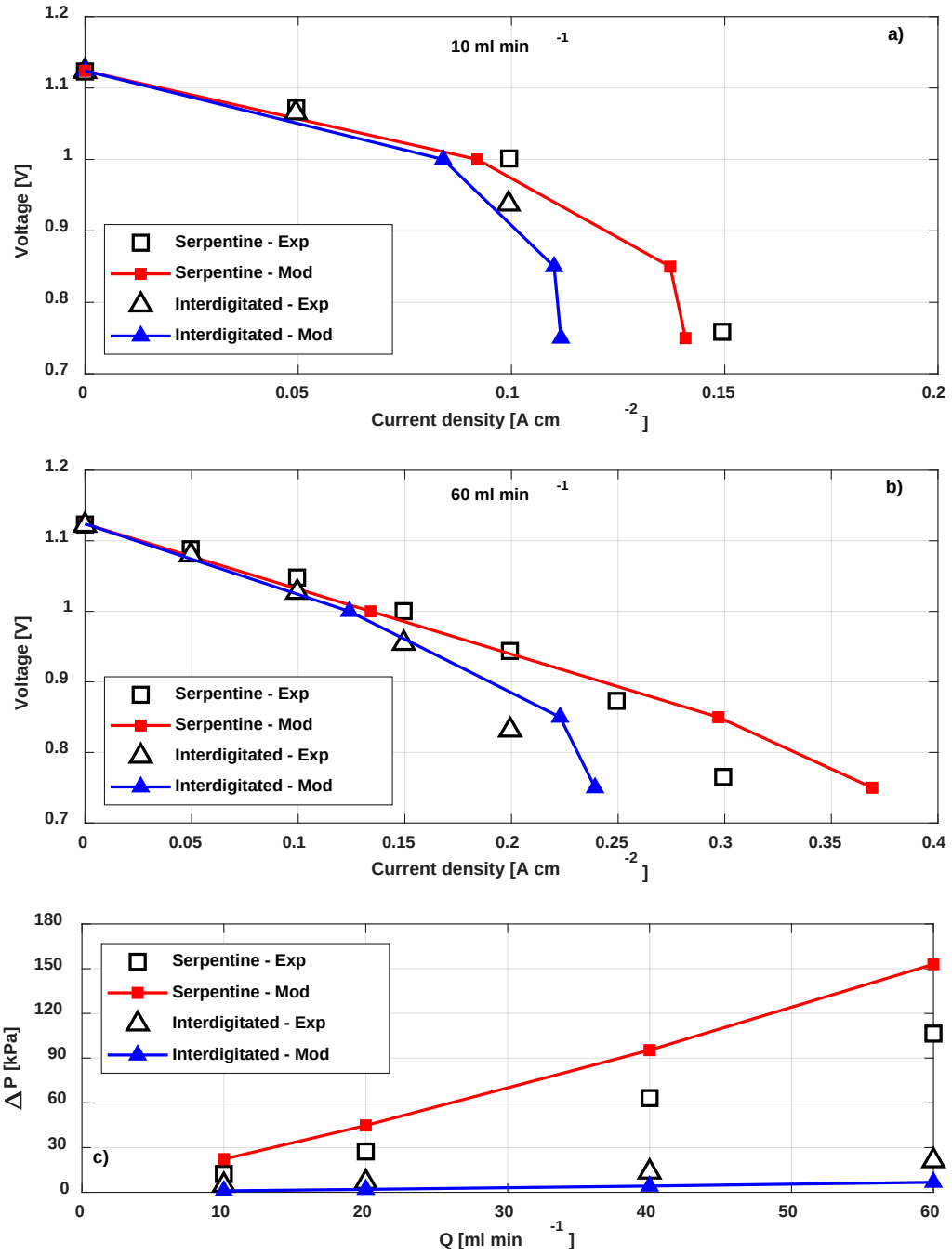

Fig. 4 – Comparison between simulation and experiments: a) polarization curves at 10 ml min^{-1} and SoC 0.6; b) polarization curves at 60 ml min^{-1} and SoC 0.6; c) pressure drops.

Since the developed model reproduced the experimentally obtained values over a wide range of operating conditions and with different flow-field configurations, it can be used as a diagnostic tool to provide insight into the physical phenomena that determine VRFB performance at the local level.

4.2.2 Local distribution of the reaction rate

Figure 5 illustrates the distribution of reaction rates in a plane at the half-height of the electrode. For the serpentine flow field (Fig. 5a), a strongly heterogeneous distribution of the reaction rate was observable: maxima were present under the ribs between two adjacent channels far away from the bends, while minima were observed under the ribs close to the bends. The simulation of the interdigitated flow field predicted a more uniform reaction rate distribution. However, the central digits do not receive a high flow rate from the distribution channel, leading to a lower reaction rate in the middle of the active area of the cell.

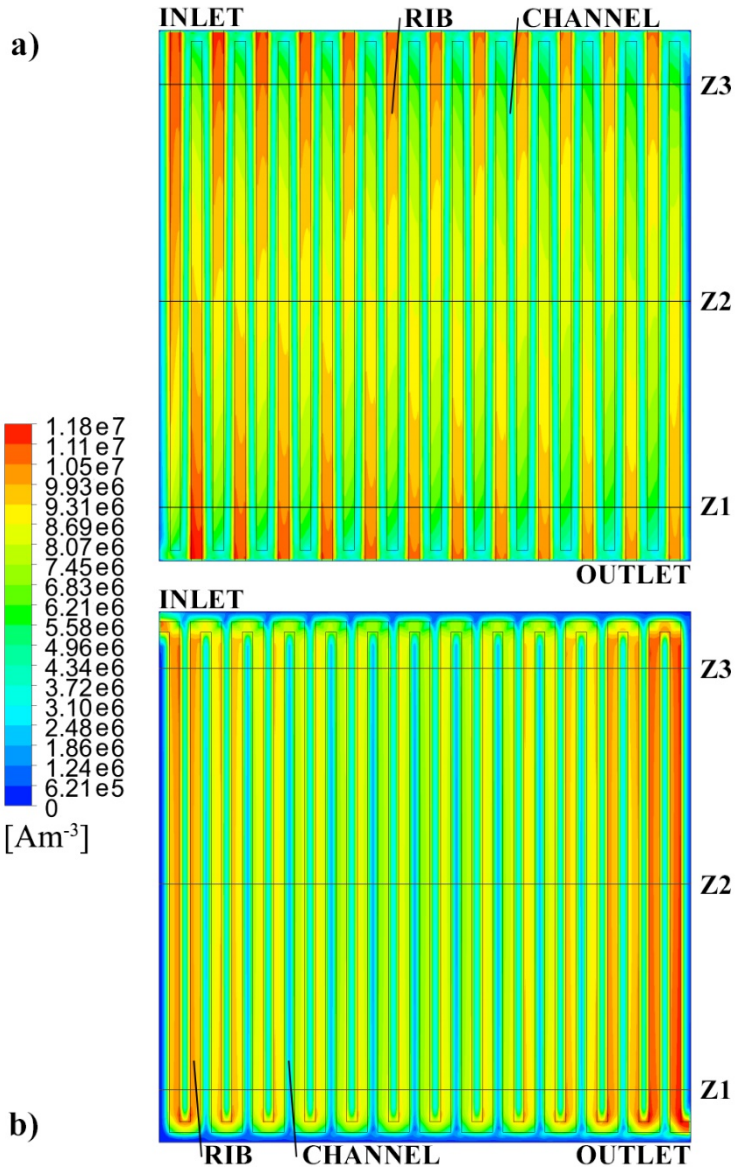

Fig. 5 – Simulated reaction rate at 0.15 A cm^{-2}, 20 ml min^{-1}, and SoC 0.6: a) single serpentine geometry; b) interdigitated geometry.

The above-mentioned considerations were valid throughout the thickness of the electrode. The zones under the ribs experienced a higher reaction rate, which was uniform in the case of the interdigitated geometry. Cross-sections of the variation of the reaction rate in the y-direction along the three lines in the x-direction (Z_1, Z_2, and Z_3 of Fig. 5) are shown in Fig. 6.

Figure 6a illustrates the reaction rate distribution throughout the entire depth of the electrode along the three lines in the x-direction, Z_1, Z_2, and Z_3. The white squares correspond to the ribs, while the grey squares represent the channels. In the serpentine geometry, it is noteworthy that the points at which the reaction rate exhibits a high value along Z_1 correspond to points with low reaction rate values along Z_3. The opposite occurs at points at which Z_3 shows a reaction rate. The reaction rate decreases under the rib always occur close to a channel bend, where the pressure drop between two adjacent channels is limited. This suggests that this behaviour results from the presence of under-the-rib fluxes. In contrast, in the Z_2 plane the reaction rate is more uniform, exhibiting only a slight increase under the ribs.

The reaction rate distribution of the interdigitated distributors is depicted in Fig. 6b. The grey squares labelled “Feed” indicate the feeding channels, and the unlabelled grey squares represent the discharge channels. The interdigitated distributor exhibits a more uniform distribution of reaction rates between channels, but the maximum values are considerably lower compared to those of the single serpentine geometry (Fig. 6a). Accordingly, in the single serpentine geometry, the reaction rate increases occur under the ribs (white squares), but the differences among the Z_1, Z_2, and Z_3 planes were less significant, due to the parallel connection among the feeding channels. In the interdigitated flow field, the intensity of the reaction rate under the ribs tends to decrease when moving from the inlet to the centre of the cell, leading to poor performance in the centre region, as also illustrated above in Fig. 5b.

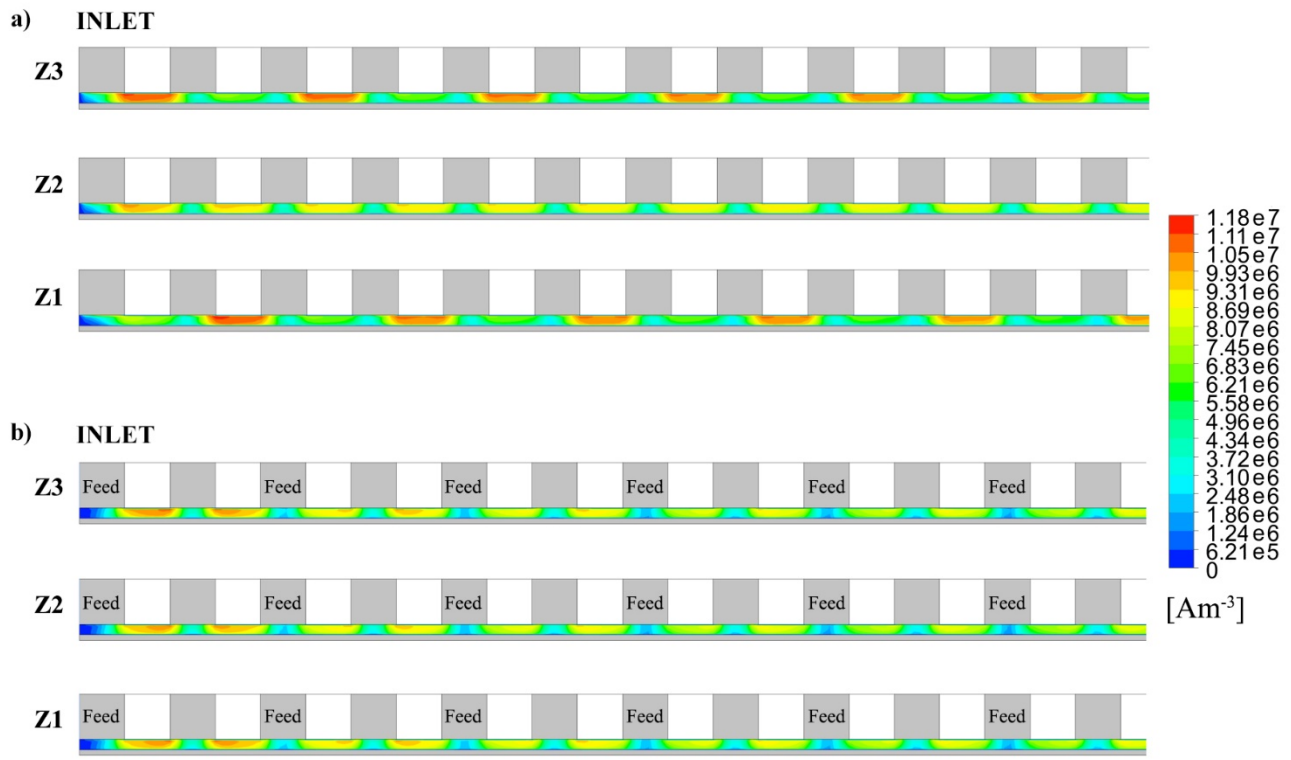

Fig. 6 – Simulated reaction rate in the y-direction at 0.15 A cm^{-2}, 20 ml min^{-1} and SoC 0.6: a) single serpentine flow field; b) interdigitated flow field. Only the region close to the inlet of the cell is represented.

The increased reaction rate under certain ribs can be explained by the presence of under-the-rib fluxes, as reported in . Under-the-rib fluxes are bypass flows under the ribs, which are promoted by the pressure gradients between consecutive channels. The under-the-rib fluxes, along with the velocities in the porous electrodes, are reported and described below.

Other conclusions about the heterogeneity of the state of charge inside the electrode can be drawn from the analysis of the contours shown in Fig. 7. The serpentine flow field results in a highly heterogeneous distribution of the reactant concentrations, with a clear reduction in the state of charge from the inlet to the outlet of the distributor. The use of an interdigitated geometry can lead to a higher homogeneity of the SoC, as shown in Fig. 7b, due to the alternating layout of the inlet and outlet branches of the distributor. For both the geometries, it is possible to observe that the reaction rate shown in Fig. 5 is the result of the interplay between the state

of charge distribution and the velocity field reported in Appendix B, revealing the strong influence of the flow field on heterogeneity during operation.

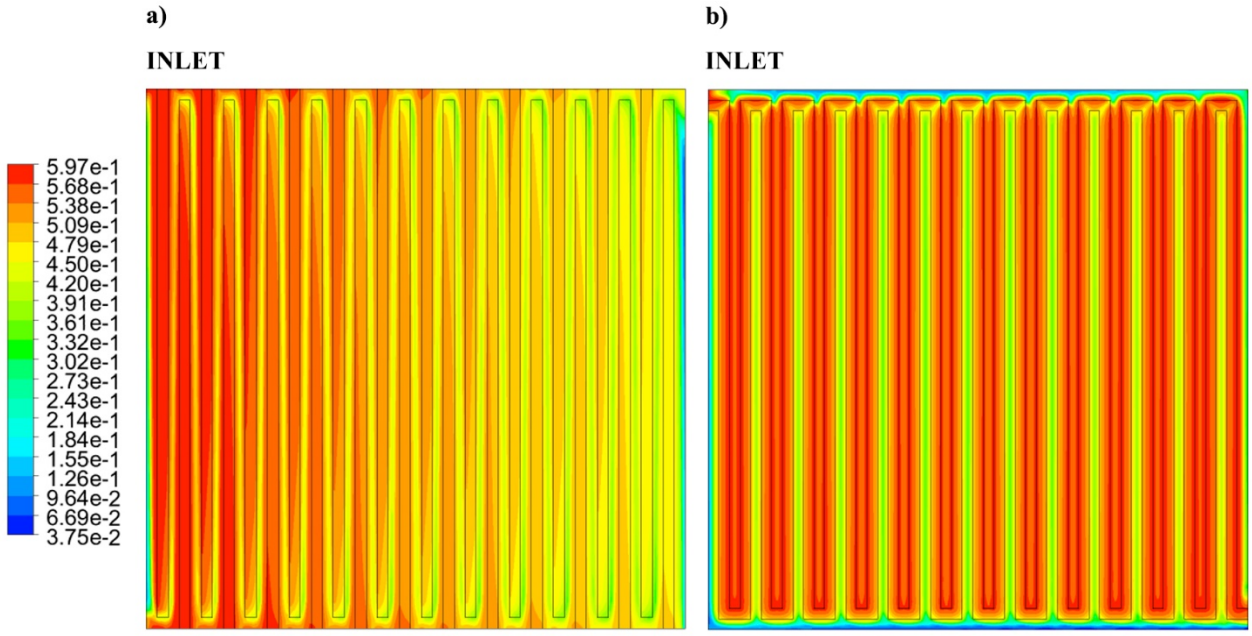

Fig. 7 – Simulated state of charge distribution at 0.15 A cm^{-2}, 20 ml min^{-1}, and SoC 0.6: a) single serpentine flow field; b) interdigitated flow field.

The development of a validated CFD model allows the contribution of the diffusion of the charged particles to the source term S_R of the protonic charge balance equation (Eq. 13) to be isolated from those of the migrative and convective effects. As shown in Fig. 8, the contribution of diffusion in the serpentine flow field is higher in the regions under the channel, in agreement with the distribution of the reaction rate shown in Fig. 5. Moreover, the magnitude of the contribution is uniform in the direction perpendicular to the channel. For the interdigitated geometry, the diffusion term is most influential under the channels of the outlet branches of the distributor, and its contribution is stronger in the central part of the cell, confirming the results presented in Fig. 5 and discussed before.

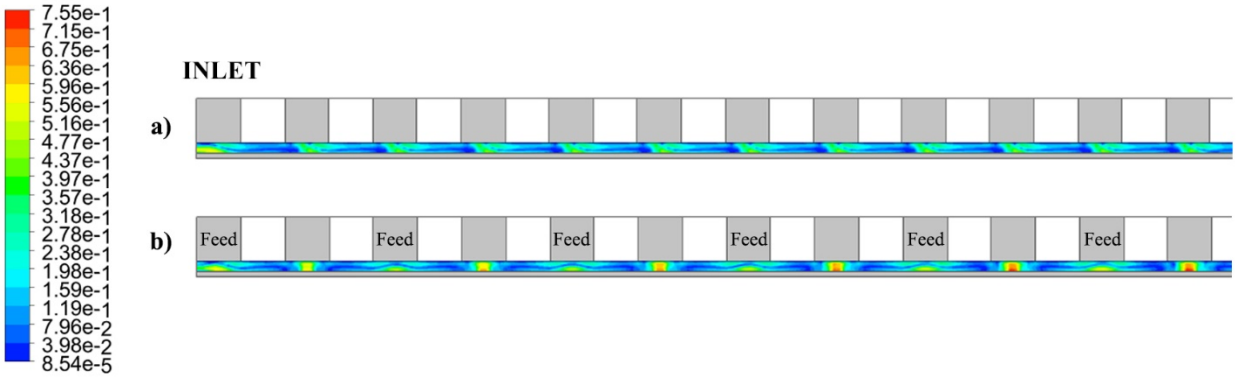

Fig. 8 – Simulated ratio between the diffusive term of Eq. 16 and the total current in the y-direction at 0.15 A cm^{-2}, 20 ml min^{-1}, and SoC 0.6: a) single serpentine flow field; b) interdigitated flow field.

4.2.3 Under-the-rib fluxes and velocities in the porous electrodes

Figure 9 illustrates the streamlines of the fluxes in the inlet region of the serpentine and interdigitated flow fields. Comparing these simulation values with the reaction rates shown in Fig. 5, the coupling between the fluxes under the ribs and the increase in the reaction rate is evident. In the single serpentine flow field, the high velocities in the distribution channel lead to increased pressure drops between consecutive channels, enhancing the under-the-rib fluxes far from the channel curves. At the channel bends, the pressure drops between the channels are limited, resulting in low velocities under the ribs. For the interdigitated geometry, the velocities in the individual distribution channels are lower than those for the serpentine flow field. This results in lower pressure drops that are more homogeneous between adjacent channels due to the parallel electrolyte feeding.

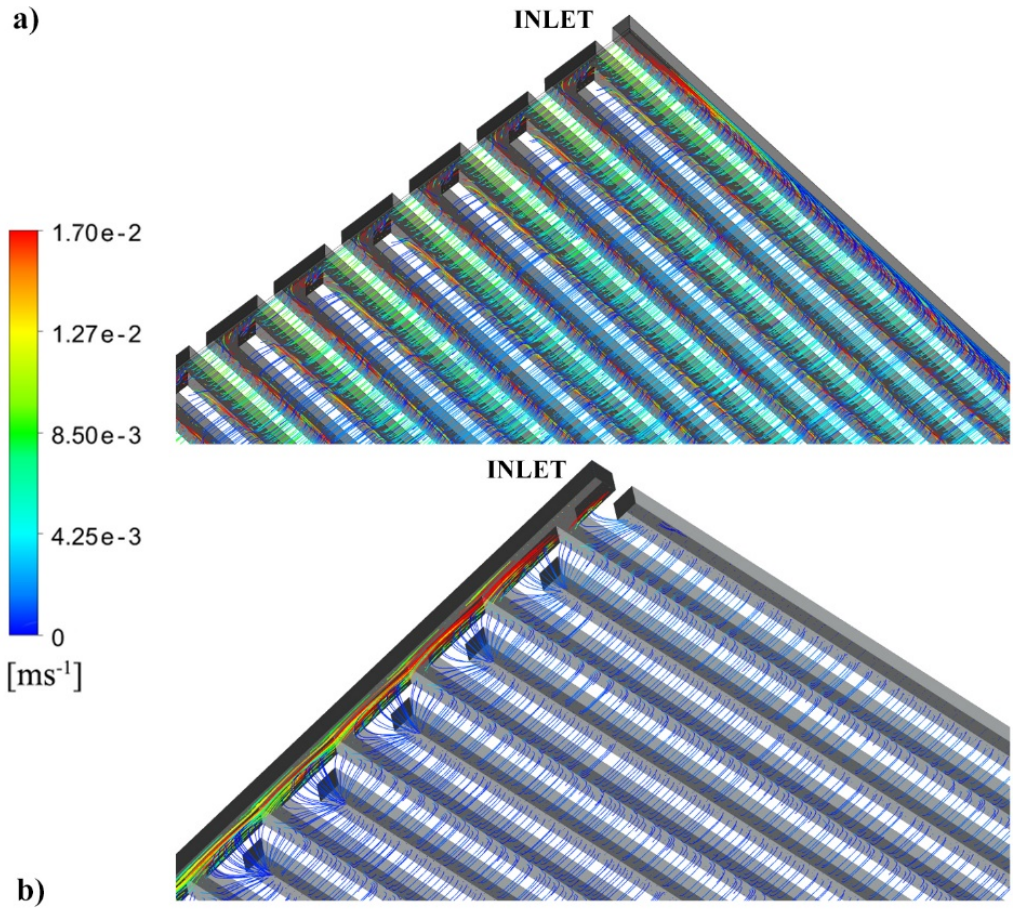

Fig. 9 – Streamlines at 0.15 A cm^{-2}, 20 ml min^{-1}, and SoC 0.6: a) single serpentine geometry; b) interdigitated geometry.

The presence of the fluxes under the ribs is consistent with the distributions of velocities in the porous electrodes, which are shown in Fig. 10 for the three lines along the y-direction lines Z_1, Z_2, and Z_3. The electrolyte velocity in the porous medium is very low, typically not higher than 4% and 1% of the inlet velocity (0.34 m s^{-1}) in the serpentine and interdigitated flow fields, respectively. Due to the bypass flow of the electrolyte, the velocity is higher under the ribs than under the distribution channels in both distributors. In the interdigitated flow field, there is almost no difference between the velocities evaluated along the lines Z_1, Z_2, and Z_3 (Fig. 10c and 10d). In contrast, in the serpentine flow field, the velocity distribution is highly heterogeneous (Fig. 10a and 10b); the maxima under the ribs along the line Z_1 correspond to local minima along Z_3 due to the presence of the bends connecting the channels (i.e., the low pressure drop

between adjacent channels). Along line Z_2, the distribution of velocities under the ribs is nearly homogeneous, leading to a more uniform reaction rate distribution (Fig. 5a); the main differences in this velocity distribution are observed between the under-channel and under-rib regions.

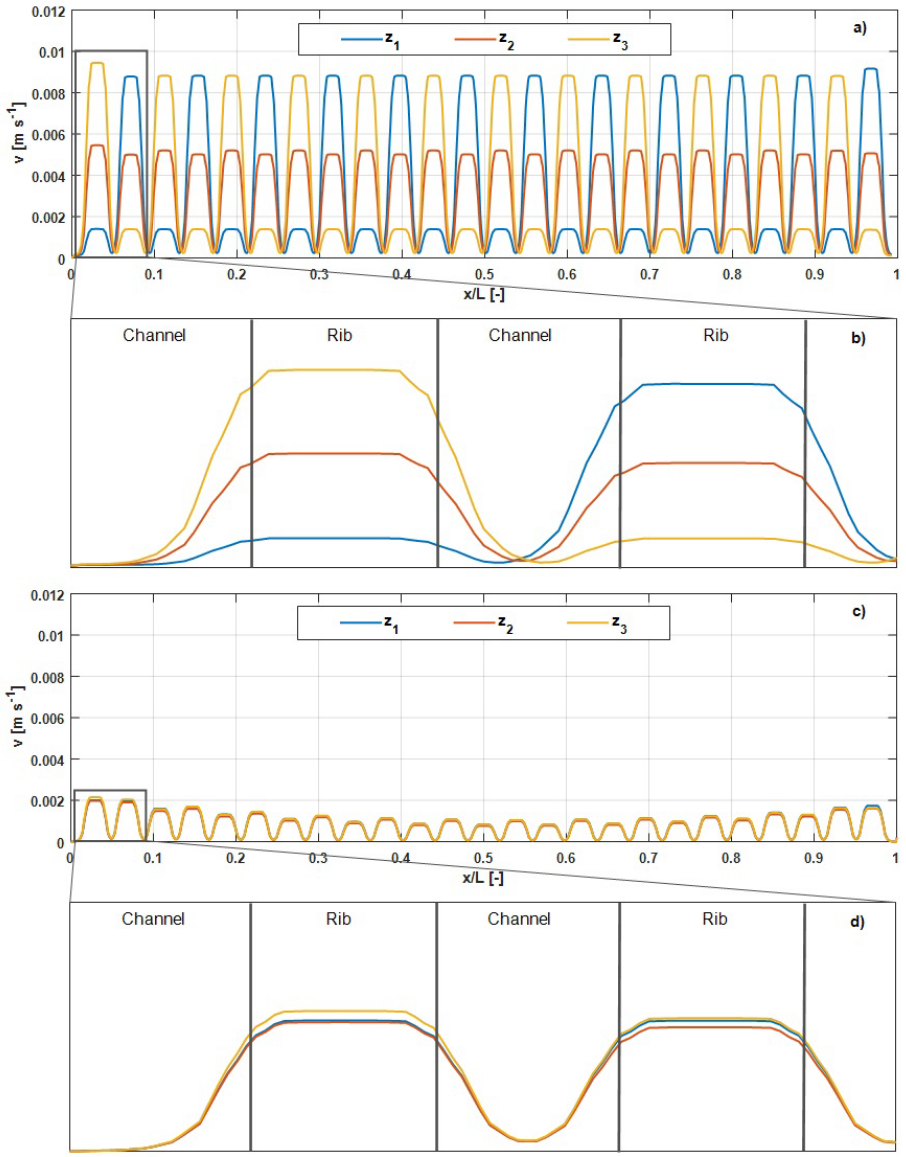

Fig. 10– Velocities in the porous electrode at 20 ml min^{-1}, 0.15 A cm^{-2}, and SoC 0.6 (zero at channel inlet, one at channel outlet): a) single serpentine flow field; b) magnified view of the rib and channel positions; c) interdigitated flow fields; d) magnified view of the rib and channel positions.

The results presented in this section are consistent with the findings reported in [26], in which the authors utilized the thermal visualization technique and reported that certain zones under

the rib of two consecutive channels experience higher velocities, leading to differences in local operation over the active area.

Considering the strong influence of the velocity distribution in the channel and in the porous medium, flow field optimization involves a trade-off between high velocities (i.e. high reaction rates) and low pressure drops (i.e. reduced auxiliary power consumption). As previously discussed in the literature [16,25,29], flow field optimization is further complicated by the interplay among other system properties, such as the active area, electrolyte typology, electrode morphology, [30,31] and nominal operating conditions.

Since the developed model has been extensively validated, it can be used as tool to provide insight into the interaction between the fluid dynamics and electrode morphology, as presented in the next section.

4.2.4 Sensitivity analysis

A sensitivity analysis was performed by changing the electrode thickness and permeability in order to elucidate the effect of the interaction between the flow field geometry and the electrode morphology. In one case, the electrode thickness was doubled, while in a different simulation the permeability was set to 67% of the original value. Doubling the thickness of the porous medium resulted in a reduction of the average volumetric reaction rate and of its heterogeneity inside the electrode. However, the profiles were qualitatively similar to those of the initial simulations, with higher reaction rates under the rib areas and lower reaction rates under the channels, as highlighted in Fig. 11a-b. The reduction of heterogeneity was particularly evident for the interdigitated geometry, for which the reduction of the reaction rate towards the centre of the cell was mitigated. Analysis of the distribution of SoC at the half-height of the electrode (Fig. 11c-d) revealed greater inhomogeneity with increased discharge of the

electrolyte along the serpentine channel and towards the centre of the cell in the interdigitated geometry.

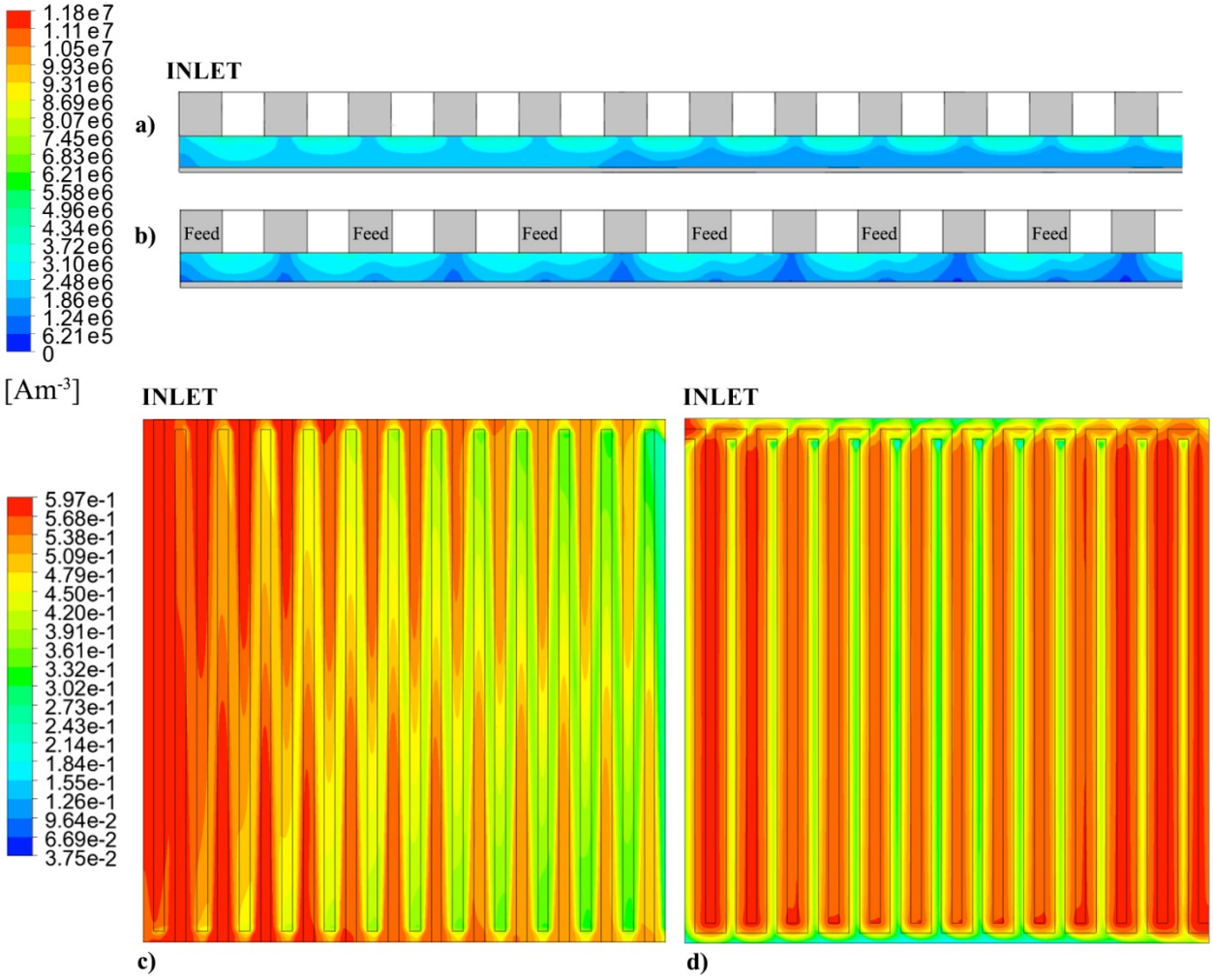

Fig. 11– Sensitivity analysis of the electrode thickness at 20 ml min^{-1}, 0.15 A cm^{-2}, and SoC 0.6: simulated reaction rate in the y-direction with a) single serpentine and b) interdigitated geometries; simulated state of charge distributions for the c) single serpentine and d) interdigitated geometries.

In terms of overall battery performance, the thicker electrode enhanced the performance for both flow fields. A greater gain was obtained for the interdigitated flow field; since the electrolyte is forced to pass inside the electrode, the higher active area resulting from the higher thickness increased the performance of the interdigitated field to equal that of the serpentine configuration, as shown in Table 3. However, mass transport issues must be considered when

increasing the electrode thickness; above a threshold value of thickness, the performance would decline [32].

Table 3 – Operating voltages used in the sensitivity analysis.

	Base case	**Thickness x 2**	**% Gain**
Serpentine	0.94 V	0.984 V	4.7 %
Interdigitated	0.85 V	0.987 V	16.1 %

Under the investigated conditions, reducing the permeability did not have any relevant effects on the distribution of the reaction rate and of the state of charge inside the electrode in terms of the overall battery performance.

5. Conclusions

In the present work, a 3D CFD model of a vanadium redox flow battery in the half-cell configuration was developed and validated in order to provide insight into the most relevant physical phenomena in terms of system performance and local heterogeneity during operation. The developed model was used to simulate both single serpentine and interdigitated flow fields with the same dimensions and active area (25 cm^2) as those used in the experiments. The adoption of the half-cell configuration allows the negative electrode to be considered as a pseudo-reference electrode with negligible potential loss, leading to a reduction in computational time and the number of fitting parameters, which can be determined with a reduced uncertainty. Using the same physical parameters, the model was validated at different flow rates for both electrolyte distributors. The agreement between the model and the experiments was acceptable, and therefore the model can be used to locally analyse the physical phenomena that regulate system performance.

The main conclusions of the work are the following:

- In all the investigated operating conditions at fixed electrolyte flow rates, both the experiments and simulations indicated that the single serpentine distributor showed better performance. However, the pressure drops associated with this geometry drastically increase with the flow rate, leading to a pressure drop of nearly 110 kPa at 60 ml min^{-1}, which was considerably higher than the pressure drop of 25 kPa observed for the interdigitated geometry.
- Considering the contribution of auxiliaries, at high flow rate and low operating current the interdigitated geometry outperformed the single serpentine geometry, highlighting the importance of comparing different distributors at a given pressure drop value, rather than at a constant flow rate.
- Both the serpentine and interdigitated flow fields exhibited increased reaction rate under the ribs, which was induced by bypass flows between channels. Flow stream visualizations and the local velocities in the porous medium evidenced the strong coupling between these fluxes and the reaction rate.
- In the serpentine geometry, the reaction rate distribution was highly heterogeneous due to the high pressure drops between adjacent channels that are not connected by a bend. As a result, the under-the-rib flux mechanism was only enhanced in certain regions of the cell active area.
- In the interdigitated geometry, due to the low velocity in the porous electrode induced by the parallel feeding of distribution channels, the reaction rate was more homogeneous.
- Both flow field configurations experienced electrolyte starvation in local regions of the cell active area. In the serpentine configuration, the region near the outlet of the channel was characterised by a low concentration of reactants because of depletion along the

distributor, while in the interdigitated configuration, the porous media under the outlet branches of the flow field results to be fed by discharged electrolyte due to the high conversion obtained under the rib.

- The strong interplay between the morphological properties of the electrode and the flow field layout was highlighted and further investigated through a sensitivity analysis, which provided insight towards the optimization of the coupling between electrodes and the geometries of distributors.

In future work, the developed model will be used as a tool to design flow field distributors as a function of the electrode morphology, optimising the trade-off between increasing the under-the-rib fluxes and reducing the pressure drops.

Acknowledgement

This work was funded by Fondi di Ateneo per la Ricerca di Base of Politecnico di Milano.

References

[1] Alotto P, Guarnieri M, Moro F. Redox flow batteries for the storage of renewable energy: A review. Renew Sustain Energy Rev 2014;29:325–35. doi:10.1016/j.rser.2013.08.001.

[2] Soloveichik GL. Flow Batteries: Current Status and Trends. Chem Rev 2015;115:11533–58. doi:10.1021/cr500720t.

[3] Parasuraman A, Lim TM, Menictas C, Skyllas-Kazacos M. Review of material research and development for vanadium redox flow battery applications. Electrochim Acta 2013;101:27–40. doi:10.1016/j.electacta.2012.09.067.

[4] Weber AZ, Mench MM, Meyers JP, Ross PN, Gostick JT, Liu Q. Redox flow batteries: A review. J Appl Electrochem 2011;41:1137–64. doi:10.1007/s10800-011-0348-2.

[5] Wu M, Liu M, Long G, Wan K, Liang Z, Zhao TS. A novel high-energy-density positive electrolyte with multiple redox couples for redox flow batteries. Appl Energy 2014;136:576–81. doi:10.1016/j.apenergy.2014.09.076.

[6] Chakrabarti MH, Brandon NP, Hajimolana SA, Tariq F, Yufit V, Hashim MA, et al. Application of carbon materials in redox flow batteries. J Power Sources 2014;253:150–66. doi:10.1016/j.jpowsour.2013.12.038.

[7] Zakeri B, Syri S. Electrical energy storage systems: A comparative life cycle cost analysis. Renew Sustain Energy Rev 2015;42:569–96. doi:10.1016/j.rser.2014.10.011.

[8] Zeng YK, Zhao TS, An L, Zhou XL, Wei L. A comparative study of all-vanadium and iron-chromium redox flow batteries for large-scale energy storage. J Power Sources 2015;300:438–43. doi:10.1016/j.jpowsour.2015.09.100.

[9] Zheng Q, Li X, Cheng Y, Ning G, Xing F, Zhang H. Development and perspective in vanadium flow battery modeling. Appl Energy 2014;132:254–66. doi:10.1016/j.apenergy.2014.06.077.

[10] Oh K, Yoo H, Ko J, Won S, Ju H. Three-dimensional, transient, nonisothermal model of all-

vanadium redox flow batteries. Energy 2015;81:3–14. doi:10.1016/j.energy.2014.05.020.

[11] Ma X, Zhang H, Xing F. A three-dimensional model for negative half cell of the vanadium redox flow battery. Electrochim Acta 2011;58:238–46. doi:10.1016/j.electacta.2011.09.042.

[12] Wang Y, Cho SC. Analysis and Three-Dimensional Modeling of Vanadium Flow Batteries. J Electrochem Soc 2014;161:A1200–12. doi:10.1149/2.0061409jes.

[13] Chen JQ, Wang BG, Lv HL. Numerical Simulation and Experiment on the Electrolyte Flow Distribution for All Vanadium Redox Flow Battery. Adv Mater Res 2011;236–238:604–7. doi:10.4028/www.scientific.net/AMR.236-238.604.

[14] Ozgoli HA, Elyasi S, Mollazadeh M. Hydrodynamic and electrochemical modeling of vanadium redox flow battery. Mech Ind 2015;16:201. doi:10.1051/meca/2014071.

[15] Yin C, Gao Y, Guo S, Tang H. A coupled three dimensional model of vanadium redox flow battery for flow field designs. Energy 2014;74:886–95. doi:10.1016/j.energy.2014.07.066.

[16] Xu Q, Zhao TS, Leung PK. Numerical investigations of flow field designs for vanadium redox flow batteries. Appl Energy 2013;105:47–56. doi:10.1016/j.apenergy.2012.12.041.

[17] Yufit V, Hale B, Matian M, Mazur P, Brandon NP. Development of a Regenerative Hydrogen-Vanadium Fuel Cell for Energy Storage Applications. J Electrochem Soc 2013;160:A856–61. doi:10.1149/2.086306jes.

[18] Pezeshki AM, Sacci RL, Delnick FM, Aaron DS, Mench MM. Elucidating effects of cell architecture, electrode material, and solution composition on overpotentials in redox flow batteries. Electrochim Acta 2017;229:261–70. doi:10.1016/j.electacta.2017.01.056.

[19] Zago M, Casalegno A. Physically-based impedance modeling of the negative electrode in

All-Vanadium Redox Flow Batteries: insight into mass transport issues. Electrochim Acta 2017;248:505–17. doi:10.1016/j.electacta.2017.07.166.

[20] Dewage HH, Yufit V, Brandon NP. Study of Loss Mechanisms Using Half-Cell Measurements in a Regenerative Hydrogen Vanadium Fuel Cell. J Electrochem Soc 2016;163:A5236–43. doi:10.1149/2.0301601jes.

[21] Ashraf Gandomi Y, Aaron DS, Mench MM. Coupled Membrane Transport Parameters for Ionic Species in All-Vanadium Redox Flow Batteries. Electrochim Acta 2016;218:174–90. doi:10.1016/j.electacta.2016.09.087.

[22] Knehr KW, Agar E, Dennison CR, Kalidindi AR, Kumbur EC. A Transient Vanadium Flow Battery Model Incorporating Vanadium Crossover and Water Transport through the Membrane. J Electrochem Soc 2012;159:1446–59. doi:10.1149/2.017209jes.

[23] Zhou XL, Zhao TS, An L, Zeng YK, Yan XH. A vanadium redox flow battery model incorporating the effect of ion concentrations on ion mobility. Appl Energy 2015;158:157–66. doi:10.1016/j.apenergy.2015.08.028.

[24] Schmal D, Van Erkel J, Van Duin PJ. Mass transfer at carbon fibre electrodes. J Appl Electrochem 1986;16:422–30. doi:10.1007/BF01008853.

[25] Houser J, Pezeshki A, Clement JT, Aaron D, Mench MM. Architecture for improved mass transport and system performance in redox flow batteries. J Power Sources 2017;351:96–105. doi:10.1016/j.jpowsour.2017.03.083.

[26] Houser J, Clement J, Pezeshki A, Mench MM. Influence of architecture and material properties on vanadium redox flow battery performance. J Power Sources 2016;302:369–77. doi:10.1016/j.jpowsour.2015.09.095.

[27] Kumar S, Jayanti S. Effect of flow field on the performance of an all-vanadium redox flow battery. J Power Sources 2016;307:782–7. doi:10.1016/j.jpowsour.2016.01.048.

[28] Lei Y, Zhang BW, Bai BF, Zhao TS. A transient electrochemical model incorporating the

Donnan effect for all-vanadium redox flow batteries. J Power Sources 2015;299:202–11. doi:10.1016/j.jpowsour.2015.08.100.

[29] Mohamed MR, Leung PK, Sulaiman MH. Performance characterization of a vanadium redox flow battery at different operating parameters under a standardized test-bed system. Appl Energy 2015;137:402–12. doi:10.1016/j.apenergy.2014.10.042.

[30] Wang Q, Qu ZG, Jiang ZY, Yang WW. Experimental study on the performance of a vanadium redox flow battery with non-uniformly compressed carbon felt electrode. Appl Energy 2018;213:293–305. doi:10.1016/j.apenergy.2018.01.047.

[31] Wang Q, Qu ZG, Jiang ZY, Yang WW. Numerical study on vanadium redox flow battery performance with non-uniformly compressed electrode and serpentine flow field. Appl Energy 2018;220:106–16. doi:10.1016/j.apenergy.2018.03.058.

[32] Liu QH, Grim GM, Papandrew AB, Turhan A, Zawodzinski TA, Mench MM. High Performance Vanadium Redox Flow Batteries with Optimized Electrode Configuration and Membrane Selection. J Electrochem Soc 2012;159:A1246–52. doi:10.1149/2.051208jes.

[33] Rahman F, Skyllas-Kazacos M. Solubility of vanadyl sulfate in concentrated sulfuric acid solutions. J Power Sources 1998;72:105–10. doi:10.1016/S0378-7753(97)02692-X.